Annals of Nuclear Energy 202 (2024) 110468

Contents lists available at ScienceDirect

Annals of Nuclear Energy

journal homepage: www.elsevier.com/locate/anucene

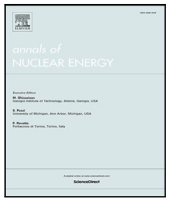

Influence of different thermodynamic parameters on variation across the aerosol size spectrum

Y. Wu [b,*], M. Klauck [b], K. Trollmann [b], H.-J. Allelein [a,b]

[a] RWTH Aachen University, 52056 Aachen, Germany
[b] Forschungszentrum Jülich GmbH, 52425 Jülich, Germany

ARTICLE INFO

Keywords:
Source term
Experimental research
Aerosol size spectra
In-/soluble aerosols
Multi-component aerosols

ABSTRACT

During a severe accident in a nuclear power plant, fission products can be released into the containment in the form of radioactive aerosols. The behavior of these aerosols is influenced by various thermodynamic parameters, including temperature, pressure, and relative humidity. Changes in these parameters can impact the aerosol size spectrum, leading to variation in aerosol transport and deposition. Having a comprehensive grasp of how thermodynamic parameters impact change in the aerosol size spectrum is crucial for managing and mitigating the consequences of a severe accident, as it allows for better prediction of aerosol behavior and appropriate interventions. A series of experimental works on in-/soluble aerosols and their mixtures has been carried out using the IN–EX facility located at the Forschungszentrum Juelich the Germany. The changes in the aerosol size spectrum of SnO_2 , CsI and two different mass composition mixtures (SnO_2 : CsI = 7:3 or 4:6) under various thermodynamic conditions are discussed and analyzed. The results show that increasing the temperature leads to a broader aerosol spectrum for SnO_2 , but not for CsI aerosols. With the increasing pressure, the aerosol size spectrum shifts towards smaller particles for CsI, but not for SnO_2 . Furthermore, increasing the relative humidity causes the aerosol size spectrum of both SnO_2 and CsI particles to shift towards larger particles, whereas CsI particles are more pronounced. The behavior of such mixtures relies on the composition of the primary substance within it. These findings provide robust information for improving the strategies of severe accident management.

1. Introduction

In the process of a loss of coolant accident (LOCA) in a nuclear power plant (NPP), fission products in the form of airborne aerosols may be transported into the containment. The thermodynamic conditions change dramatically depending upon the type of NPP undergoing an LOCA. For instance, in a pressurized water reactor, because of the rupture of the main coolant pipe, vapor with the radioactive source term will be released into the containment. Pressure in it can increase up to 5.69 bar, the temperature may rise to 145 °C, and the relative humidity may increase to more than 100% (Ziegler and Allelein, 2013). If a hydrogen deflagration occurs at the same time, the pressure may further increase and exceed the design pressure. There is even the risk of a failure of the containment, the last barrier of an NPP against the releasing of the radioactive source term, resulting in the release of radioactive aerosols into the environment and threatening human health. All changes in thermodynamic conditions bring about unknown changes in the aerosol spectrum, which in turn affect the behavior of the aerosol in the containment (Dehbi et al., 1997; Wu et al., 2022a,b), such as depletion and interaction behavior, pool scrubbing efficiency, etc. Hence, it is essential to investigate the influence of thermodynamic parameters on the variation of aerosol-sized spectra.

A large number of experimental studies over the last few decades have investigated on aerosol behavior, such as deposition, sedimentation, agglomeration, and diffusion, by measuring the variation of aerosol size distribution with time under different thermodynamic conditions. A solid knowledge of aerosol depletion and deposition behavior has been gained through a series of projects, such as the DEMONA, VANAM, KAEVER, THAI, and SAAB experiments (Fromentin et al., 1988; Firnhaber et al., 1996; Kanzleiter et al., 1991; Scheibel et al., 1992, 1993, 1994; Firnhaber et al., 2002; Gupta, 2017; Gupta et al., 2015; Kobalz and Allelein, 2017). All of these projects have investigated aerosol behavior, including experimental measurements of the particle size distribution of aerosols over depletion times, and have provided detailed data for the improvement of modeling, some of which have also contributed to the international standard problem (ISP) in the nuclear field (Firnhaber et al., 1996, 2002). The effect

* Corresponding author.
E-mail address: yihui.wu@rwth-aachen.de (Y. Wu).

https://doi.org/10.1016/j.anucene.2024.110468
Received 18 September 2023; Received in revised form 6 March 2024; Accepted 7 March 2024
Available online 18 March 2024

Nomenclature

τ	Particle relaxation time in [s]
$c_{O_2,dilu}$	Oxygen volume concentration of dilution air in [%]
$c_{O_2,ex}$	Exhaust oxygen volume concentration in [%]
$c_{O_2,in}$	Sampling inlet oxygen volume concentration in [%]
d	Particle diameter in [cm]
d_{max}	Upper diameter limits of a aerosol size distribution in [μm]
d_{min}	Lower diameter limits of a aerosol size distribution in [μm]
D_s	Diameter of sampling pipe in [mm]
F_{adh}	Adhesive force in [dyn]
N	Dilution ratio
Q	Sampling flow rate in [$m^3\ s^{-1}$]
$U_{0,crtical}$	Critical gas velocity for sampling in still air in [$m\ s^{-1}$]
$u_{c_{O_2,ex}}$	Uncertainty of exhaust oxygen volume concentration
$u_{dilution}$	Uncertainty of dilution ratio
$u_{O_2,dilu}$	Uncertainty of oxygen volume concentration in dilution air
$u_{O_2,in}$	Uncertainty of sampling inlet oxygen volume concentration
ACMD	Aerodynamic Count Median Diameter
AMMD	Aerodynamic Mass Median Diameter
ASNS	Atomizing Spray Nozzle System
FCVS	Filtered Containment Venting System
GSD	Geometric Standard Deviation
ISP	International Standard Problem
LOCA	Loss Of Coolant Accident
NPP	Nuclear Power Plant
PDB	Powder Dispersing with Brush
RH	Relative Humidity
RT	Room Temperature
SA	Severe Accident

of relative humidity and the type of aerosol species were the greatest concern in these projects. Detailed information on the experimental conditions of the different projects and their concerns are presented in the reference Wu et al. (2022a). Although the effects of temperature and pressure were not a major topic addressed, a large amount of measurement data was available for further analysis. Essentially, the aerosol depletion behavior under the influence of various thermodynamic parameters (temperature, pressure and relative humidity) was summarized through a systematic investigation of the SAAB project (Wu et al., 2022a,b). Furthermore, the range of aerosol particle size distribution decreases with time until the "self-preserving" point is reached, where the geometric standard deviation (GSD) of this distribution is about 1.5 (Hinds, 1999). Li et al. (2018) have studied the transportation and deposition of polydisperse micron-sized aerosol particles in a horizontal low Reynolds number turbulence channel using Direct Numerical Simulation coupled with Lagrangian Particle Tracking. Their aim was to develop a model for assessing aerosol loss and establishing the relationship with leak rate. Notably, they utilized Count Median Diameter values as input for their simulation, a parameter influenced by thermodynamic conditions in fact. Kim et al. (2016) mainly explored changes in aerosol size distribution during the operation of a Filtered Containment Venting System (FCVS) using the NAUA code. They revealed the dominant aerosol deposition mechanisms based on temperature differences between the wall and internal air through their model. However, the effect of changes in internal air temperature on changes in aerosol particle size distribution was not of concern to them. However, how the aerosol size distribution changes with the thermodynamic parameters is unclear. For example, what is the difference in aerosol particle size distribution between 60 °C and 150 °C in the containment? To the best of authors' knowledge, longitudinal comparison and analyses of aerosol spectral changes under different temperatures, pressures, and relative humidities are lacking. As the aforementioned thermodynamic conditions in a severe accident (SA) change rapidly and dramatically, an understanding about aerosol spectra changes with the thermodynamic parameters is able to assist in improving the severe accident management. It can also contribute to improving the accuracy of simulations due to more precise inputs of the aerosol distribution.

Table 1
Overview of the experimental matrix for testing the influence of thermodynamic parameters on the nuclear aerosol spectrum.

Mass ratio	T/°C			P/bar (g)		RH			
(SnO_2: CsI)	RT	60	120	3	6	dry	med	high	con
1:0 (pure SnO_2)	√	–	√	√	√	√	√	√	√
7:3	√	√	–	√	√	–	√	√	√
4:6	√	√	–	√	√	–	√	√	√
0:1 (pure CsI)	√	√	–	√	√	√	√	√	√

A series of experiments were performed at the IN–EX facility at the Forschungszentrum Jülich. The aerosol size distribution was measured under various temperature, pressure and relative humidity conditions. In the experiments, the aerosol was divided into insoluble species (SnO_2) and soluble species (CsI) in order to verify whether the solubility of aerosols would affect the results. The purpose of this paper is to report on the effect of the thermodynamic parameters on the aerosol size spectral variation observed.

2. Facility information

The main components of the IN–EX facility include the IN–EX vessel, aerosol generators, and a measurement system consisting of a sampling pipe, dilution system, and measurement instruments (here, ELPI+), as shown in Fig. 1. The IN–EX pressure vessel is capable of operating at a maximum gauge pressure of 8 bar and temperature of 200 °C. Its internal volume is 1.1 m^3, with a height of 2 m and an internal diameter of 800 mm. The vessel is equipped with an electric heating system to adjust the temperature and has a compact thermal insulation covering to maintain the temperature inside and reduce heat losses (as shown in Fig. 2). The sampling pipe, connected to the dilution system and measurement instruments, was situated at a height of 1.5 m. In our experimental design, the selection of the sampling height at 1.5 m was a thoughtful decision based on two primary considerations. Firstly, we aimed to measure the aerosol in a position where the gas flow had fully developed. Practical constraints within the IN–EX vessel limited us to measure at a maximum height of 1.5 m. Secondly, we positioned the sampling pipe in the middle of the vessel at 1.5 m to mitigate radial influences. The experimental temperatures were room temperature (RT), 60 °C, 120 °C, and 180 °C, while the pressures were tested at 0 bar, 3 bar, and 6 bar. Humidity was tested in dry (0%–30% r.h., in the following referred to as 'dry'), medium (30%–80% r.h., in the following referred to as 'med'), high (80%–100% r.h., in the following referred to as 'high'), and condensation (>100% r.h., in the following referred to as 'con') conditions. An overview of the test matrix for pure aerosols (SnO_2 and CsI) and their mixture in two mass fractions (7:3 and 6:4) is presented in Table 1.

To experimentally-investigate the impact of thermodynamic parameters on the variation of the aerosol spectrum, it is essential to

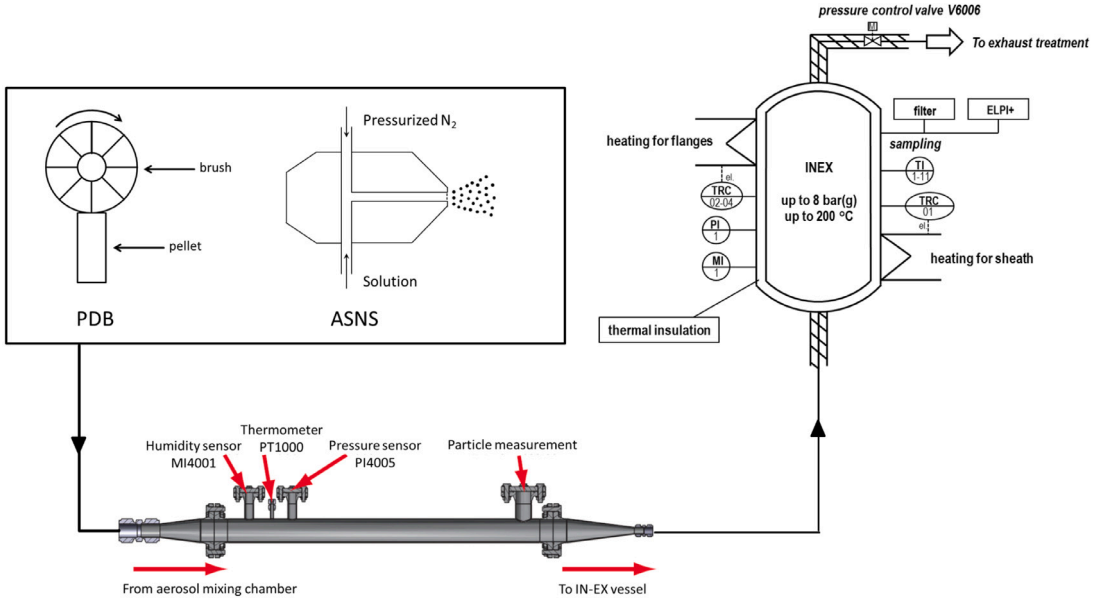

Fig. 1. IN–EX facility structure information.

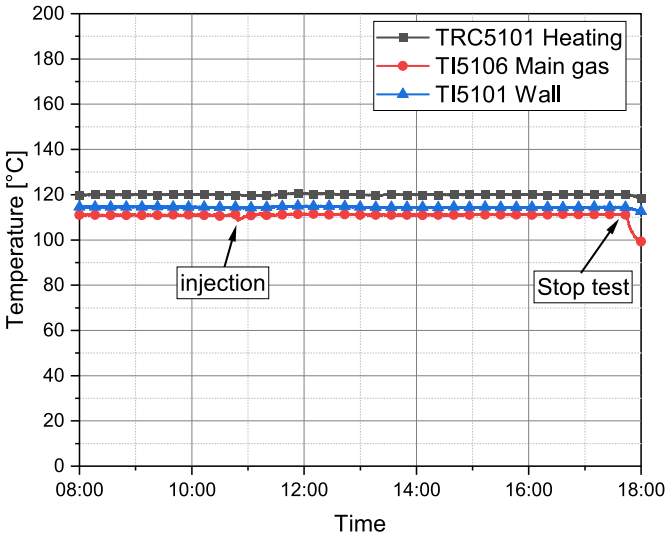

Fig. 2. Measured temperature change during the test from heating controller TRC5101 and thermocouple TI5108 for gas (heating temperature is set as 120 °C) (Wu et al., 2022a).

have a well-designed experimental procedure. As outlined in reference Wu et al. (2022a), the experimental process comprises three sequential stages: flushing, pre-conditioning (including pre-heating, pre-pressurizing, and pre-humidification), injection and measuring. The flushing stage aims to establish consistent initial conditions, particularly in terms of particle concentration, across all experiments. Pre-conditioning phase ensures that all the thermodynamic conditions in IN–EX vessel are stable before aerosol injection. In our experiments, ELPI+ was used to measure the particle size distribution of aerosols. ELPI+ is an improved type of cascade impactor, that combines electrical detection of charged particles with a low pressure cascade impactor (Keskinen et al., 1992). According to the manufacturer, this allows real-time measurements of particle size distributions in a broad particle size range from 6 nm to 10 μm with 14 particle size fractions. Moreover, ensuring the stability and reproducibility of aerosol generation, proper setting and operation of the aerosol injection, and accurate aerosol sampling, are crucial factors for obtaining reliable measurements.

2.1. Aerosol generation

At the Forschungszentrum Juelich, there are two aerosol generators, namely Powder Dispersing with a Brush (PDB) and the Atomizing Spray Nozzle System (ASNS). The PDB is specifically designed to produce insoluble aerosols, specifically SnO_2, whereas the ASNS is utilized for generating soluble aerosols such as CsI. Other studies (Wu et al., 2022a; Wu et al.) have demonstrated that the generation profile of PDB and ASNS is both stable and reproducible. Table 2 displays the Aerodynamic Mass Median Diameter (AMMD), Aerodynamic Count Median Diameter, and Geometric Standard Deviation (GSD) of the aerosol size distribution from generators. To ensure the accuracy of the results comparison, the generated size distribution curves were measured in the IN–EX vessel, thereby avoiding any influence of particle loss in the injection line. The reliability of PDB and ASNS aerosol generation, as assessed by AMMD/ACMD/GSD, is demonstrated by the relative deviations observed in repeated measurements. The results indicate that SnO_2 and CsI have comparable AMMD values, and yet CsI generates more submicron particles due to its lower ACMD values. Moreover, CsI displays a broader particle size distribution compared to SnO_2, which can be attributed to CsI having a higher GSD value than SnO_2.

2.2. Aerosol injection

Before injecting the aerosol into the IN–EX vessel, it is passed through a long injection tube for particle mixing and aerosol conditioning. However, due to the small diameter of the tube (1 inch), it is not feasible to install sensors such as thermocouples, relative humidity sensors, and pressure sensors. To overcome this, as is illustrated in Fig. 3, a diffuser is used to enlarge the diameter of the line to enable the installation of the sensors. Following the conditioning section, the diameter of the injection tube is then returned to 1 inch to maintain a consistent injection rate. However, it should be noted that due to the sudden reduction in carrier gas velocity after passing through the diffuser, large particles may not follow the gas line again due to their higher gravitational attraction, resulting in their deposition after the diffuser. One advantage is that unfocused large particles can be removed first before injecting aerosols into the vessel. Furthermore, the loss of large particles after the diffuser should be consistent, which the aerosol generation profile confirms. The injection will not begin until the vessel reaches the desired conditions of stable state, which include

Table 2
Values of AMMD, ACMD, and GSD obtained from aerosol generators.

Generators	AMMD		ACMD		GSD	
	[μm]	Deviation	[μm]	Deviation	–	Deviation
PDB (SnO_2)	1.57 ± 0.055	3.50%	0.50 ± 0.002	0.40%	1.85 ± 0.015	0.81%
ASNS (CsI)	1.59 ± 0.031	1.95%	0.37 ± 0.019	5.14%	2.01 ± 0.034	1.69%

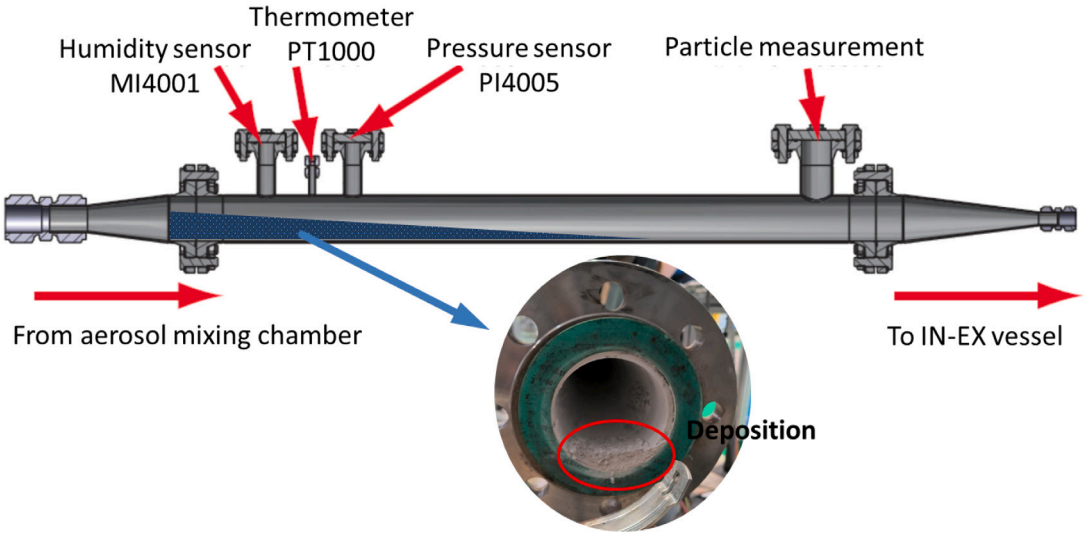

Fig. 3. Large particle deposition through the injection line.

the appropriate temperature, pressure, and relative humidity. Wu et al. (2022a) provides more detailed information regarding the distribution of temperature and changes in relative humidity within the vessel and injection line.

Once the temperature, pressure, and relative humidity within the IN-EX vessel reach the desired test conditions, the aerosol injection phase starts. In order to ensure result comparability, consistent particle generation (using ASNS and PDB) and injection procedures are employed across all experiments. ASNS uses a CsI solution (concentration approx. 34.9 w%) to generate soluble CsI particles, while PDB injects SnO_2 particles as representatives of insoluble particles into the vessel. Nitrogen (N_2) serves as the carrier gas, maintaining a constant flow rate of 20 $m^3\,h^{-1}$ throughout each experiment. The injection phase persists for 30 min in each trial, yielding particle number concentrations reaching up to 10^7 (Wu et al., 2022a).

2.3. Aerosol sampling

The process of aerosol sampling is arguably the most crucial component of the experiments, as most errors tend to occur during this phase. The accuracy of measurements can be affected by several factors, including the sampling method, setup and length of the sampling line, dilution system, and configuration of the measuring instrument. Davies (1968) suggests Eq. (1) as a criterion for selecting a sampling method based on the gas velocity in the vessel. There are two recommended approaches for sampling: if the velocity does not exceed $U_{0,crtical}$, the recommended approach is to sample in still air; otherwise iso-kinetic sampling is advised.

$$U_{0,crtical} = \frac{1}{5}\left(\frac{Q}{4\pi\tau^2}\right)^{1/3} \tag{1}$$

Calculation of the sampling flow rate Q is essential for determining the critical gas velocity $U_{0,crtical}$ and subsequently selecting the appropriate sampling method. During the IN–EX experiments, a dilution system was employed to reduce the density of measuring particles, thus preventing overloading of the ELPI+. Additionally, the sampling flow rate Q varied depending on the dilution ratio. A smaller sampling flow rate is required for accurate measurements, especially in light of the limited volume of the IN–EX vessel, which is only 1.08 m^3. As the dilution ratio increases, the sampling flow rate correspondingly decreases. Therefore, it is crucial to set a high dilution ratio to ensure the measuring accuracy. During the IN–EX experiments, the dilution ratios were set to three different values depending on the particle concentration within the vessel: approximately 8, 40, and 70. It is important to note that the dilution system assumes that particles are uniformly mixed in the mixing chamber. Any deviation from this assumption can result in a difference between the particle concentration before and after dilution. For example, if a dilution ratio of 70 is used in the IN–EX experiments, the corresponding sampling flow rate Q is 0.43 L/min. The maximum measurable particle size with ELPI+ is 10 μm, and based on this, the highest relaxation time τ is calculated to be 0.27 ms. From this, the maximal critical gas velocity $U_{0,crtical}$ is determined to be 0.39 m/s. Therefore, if the gas velocity in the IN–EX vessel exceeds 0.39 m/s, iso-kinetic sampling should be employed. During the experiments, the injected N_2 volume flow remained constant at 20 m^3/h. Under the conditions of 60°C, 0 bar, and dry during injection, the gas velocity U_0 in the IN–EX vessel was approximately 0.013 m/s. This value is significantly lower than the critical gas velocity $U_{0,crtical}$ of 0.39 m/s, indicating that sampling in still air is appropriate for the IN–EX experiments.

To ensure consistent measurement accuracy, the length of the sampling line in the IN–EX experiments remains constant to ensure that the particle loss through the line is consistent. Additionally, in order to avoid diffusion loss during sampling, it is essential that the temperature of the sampling pipe be the same as that of the particles. The orientation of the sampling pipe also affects the accuracy of the measurements. In the IN–EX experiments, the sampling pipe is placed in a horizontal direction. However, due to the gravity and inertia of large particles, they may settle on the surface of the sampling pipe or have an impacting effect at the bend. As a result, the measured particle concentration is smaller than the actual concentration. However, Davies (1968) has shown that these errors can be neglected through Eq. (2) by controlling the diameter of the sampling pipes. The lower and upper limits of

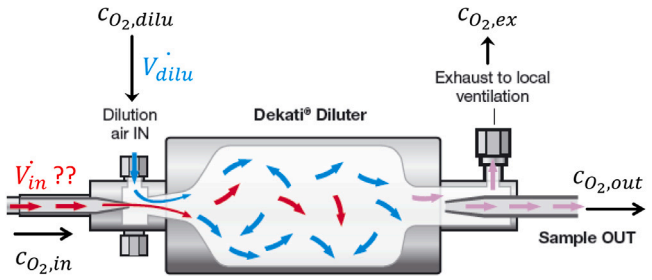

Fig. 4. Operating principle of the Dekati DI-1000.
Source: Modified from Ltd. (2018).

the three pairs of sampling pipe diameters were calculated when all dilution ratios were taken into account. The sampling pipe was suitable for all dilution ratios. Therefore, the diameter of the sampling pipe should be within the range of the highest lower and lowest upper limits for all dilution ratios. The highest lower diameter limit of the sampling pipe was found to be 9.20 mm when a dilution ratio of 8 and particle size of 10 μm were used. On the other hand, the lowest upper diameter limit was calculated to be 11.72 mm when the dilution ratio was 70 and the particle size 10 μm. As a result, a sampling pipe with a diameter of 10 mm was selected for the experiments to ensure accurate and consistent particle measurements.

$$10\left(\frac{Q\tau}{4\pi}\right)^{1/3} \le D_s \le \frac{2}{5}\left(\frac{Q}{\pi\tau g}\right)^{1/2} \tag{2}$$

As is shown in Fig. 4, the Dekati DI-1000 was applied in the experiments. To determine the dilution ratio therein, direct measurement of the inlet sampling volume flow $\dot{V}_{in}$ was not possible with the dilution system used. To address this, a gas analyzer was connected to the system to measure the exhaust oxygen volume concentration $c_{O_2,ex}$ before and during sampling, which allowed for accurate calculation of the dilution ratio (Eq. (3)) and determination of particle concentrations in the sampling line. However, reading the oxygen volume concentration values on the PC introduces a margin of uncertainty. Moreover, the uncertainty propagation of the dilution ratio is affected by slight fluctuations in the sampling and dilution gas, which can result in a variation in the dilution factor ranging from 1% to 7%, as determined by Eq. (4). For each experiment, the length of the connecting line between the dilution system and ELPI+ was held constant, and the ELPI+ settings were kept identical for experiments performed under the same conditions.

$$N = 1 + \frac{c_{O_2,ex} - c_{O_2,in}}{c_{O_2,dilu} - c_{O_2,ex}} \tag{3}$$

$$u_{dilution} = \sqrt{(f'(c_{O_2,ex})u_{c_{O_2,ex}})^2 + (f'(c_{O_2,in})u_{c_{O_2,in}})^2 + (f'(c_{O_2,dilu})u_{c_{O_2,dilu}})^2} \tag{4}$$

2.4. Aerosol evaluation

Selecting an appropriate method for evaluating the aerosol size distribution is crucial. While double logarithmic plotting is a common approach, it only displays the shape and trend of the size distribution. In our experiments, we aimed to examine changes in the aerosol size spectrum under different thermodynamic conditions. Thus, double logarithmic plotting was not suitable for our purposes. Instead, we chose to use the lower and upper limits (d_{min} and d_{max}) of the aerosol aerodynamic diameter to describe these changes. By combining these limits with the values of AMMD and GSD, we were able to gain a more complete understanding of how the thermodynamic parameters affected the changes in the aerosol size spectrum. As the aerosol size distribution typically follows a lognormal distribution, the lower and upper diameter limits could be calculated using Eqs. (5) and (6) with a confidence level of 95%. It should be noted that this range between d_{min} and d_{max} is asymmetrical. Additionally, the Hatch–Choate conversion in Eq. (7) provides insight into the relationship between AMMD, ACMD, and GSD, which can help determine the profile of the aerosol size spectrum (Hinds, 1999).

$$d_{min} = exp[lnAMMD - 2lnGSD] = AMMD/GSD^2 \tag{5}$$

$$d_{max} = exp[lnAMMD + 2lnGSD] = AMMD * GSD^2 \tag{6}$$

$$AMMD = ACMDexp(3ln^2GSD) \tag{7}$$

3. Results and discussion

A wide-ranging analysis was conducted to measure the aerosol size distribution in a series of experiments, varying the temperature, pressure, and relative humidity conditions. The measurements were carried out using pure SnO_2, CsI, and their mixtures. Based on the obtained values of the AMMD and GSD, the range of the aerosol size spectrum was determined with a 95% confidence level. The next section presents and discusses the results in detail. To account for the dynamic effects of fluid flow during the injection phase, the data used in this analysis were measured after a ten-minute period following the injection. This time delay enabled the stabilization of the system and ensured that the measured data accurately represented the steady-state conditions without the influence of transient effects. Additionally, the data collected following a one-hour depletion period offers further validation of our conclusion.

3.1. Temperature impact

Throughout the experiments, continuous electrical heating was externally applied to the injection line and vessel to maintain a constant temperature of 60 °C. It is worth to mention that the SnO_2 experiments were conducted at 120 °C while the other experiments were conducted at 60 °C due to a limitation we encountered during the experiments, i.e., our existing equipment peripherals were unable to achieve condensation conditions at 120 °C. The insulation efficiency of this heating system was documented and presented in Wu et al. (2022a). Based on the measured particle size distributions, Table 3 displays the calculated basic parameters, including AMMD, GSD, d_{min}, and d_{max}, for assessing the changes in the aerosol size spectrum. The relative errors in the table were calculated based on the aerosol generator uncertainties. It was observed that in the IN–EX experiments, when the GSD values were comparable, the AMMD values decrease with a decrease in the composition of SnO_2 in the mixture, regardless of whether the experiments were conducted at room temperature (RT) or 60 °C. For example, under RT conditions, the AMMD decreased from 1.64 to 1.17. Moreover, there were almost no significant differences in the AMMD and GSD values for CsI between RT and 60 °C.

To visually represent the change in aerosol size spectrum more clearly, the correlated values of d_{min} and d_{max} were plotted in Fig. 5. It was observed that the aerosol spectrum for SnO_2 particles widened with an increase in temperature, indicating a broader range of particle sizes. On the other hand, there were almost no significant differences observed in the aerosol size spectrum for CsI particles between the two temperatures. The mixture with a mass composition of SnO_2 to CsI at a ratio of 7:3 exhibited no significant change in d_{min}, whereas d_{max} increased at two different temperatures, indicating a shift in the aerosol spectrum towards larger particles. Conversely, for the mixture with a mass composition of 4:6, d_{max} remained unchanged, whereas d_{min} decreased, suggesting that the aerosol size spectrum widened towards finer particles at high temperatures.

As the temperature increases, the kinetic energy of particles also does, leading to more active motion and collisions amongst them. This increased kinetic energy promotes particle movement and enhances

Table 3
Impact of temperature on the aerosol size spectrum under medium humidity and atmospheric pressure.

Material	AMMD/μm		GSD		d_{min}/μm		d_{max}/μm	
	RT	60 °C	RT	60 °C	RT	60 °C	RT	60 °C
SnO_2[a]	1.64	1.82	1.60	1.96	0.64 ± 0.012	0.47 ± 0.009	4.20 ± 0.213	6.99 ± 0.363
7 : 3[b]	1.45	1.60	1.63	1.73	0.55 ± 0.0006	0.53 ± 0.001	3.85 ± 0.205	4.79 ± 0.247
4 : 6[b]	1.37	1.26	1.60	1.69	0.54 ± 0.005	0.44 ± 0.004	3.51 ± 0.179	3.60 ± 0.189
CsI	1.20	1.12	1.62	1.61	0.46 ± 0.007	0.43 ± 0.006	3.15 ± 0.165	2.90 ± 0.165

[a] SnO_2 experiments were carried out at 120 °C.
[b] The ratio is the mass composition ratio of SnO_2 to CsI.

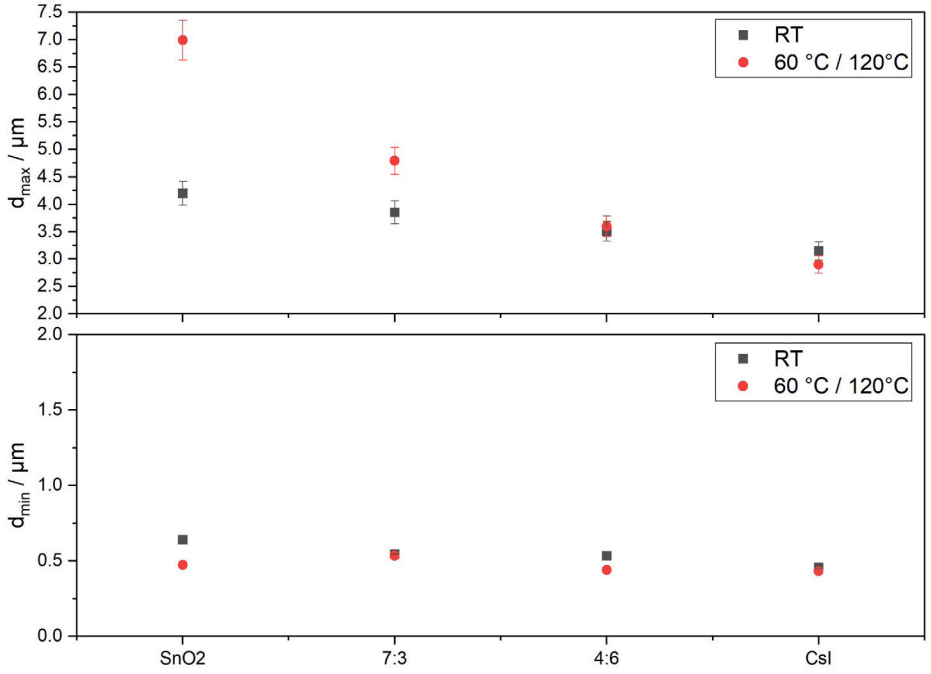

Fig. 5. Comparing the aerosol size thresholds at two different temperatures under medium humidity and atmospheric pressure.

the likelihood of particle interactions and collisions. Consequently, the aerosol particles exhibit more dynamic behavior and can be subject to agglomeration or de-agglomeration processes, resulting in changes in the aerosol size distribution and spectrum. The mechanisms of agglomeration and de-agglomeration involve particle collisions, where the particles either stick together or break apart upon impact. In the case of particles with similar sizes, it is generally assumed that they adhere together upon collision rather than breaking up (Hinds, 1999). In this paper, however, polydisperse particles with a wide size spectrum were used, and the agglomerates formed were typically porous and prone to breaking apart. Previously, particle de-agglomeration was not considered to be significant in severe accidents involving nuclear reactors. However, tests conducted in the ARTIST program have demonstrated that under SGTR conditions, it is possible for aerosol particles such as TiO_2 to deagglomerate within the tube and the expansion zone behind the tube's exit (Lind et al., 2010). Although the test velocity in our experiments was much lower than that in the ARTIST program, it still sheds a light on the consideration of de-aggregation effects in our tests. Therefore, it is essential to consider the effects of both agglomeration and de-agglomeration processes in discussion of the aerosol spectrum, even if the de-agglomeration effect is relatively weak. On the other hand, as the temperature increases, the gas expands, resulting in an increase in the diameter aerosol particles. The aerosol particle size distribution is expected to exhibit a shift towards larger particles. It is important to highlight that this phenomenon is particularly noticeable for larger aerosol particles, as the gas contribution becomes more significant.

The increase in d_{max} is a result of agglomeration or gas expansion, whereas the decrease in d_{min} can be attributed to de-agglomeration. The cumulative mass distribution of SnO_2 (left) and CsI (right) aerosols at two different temperatures in Fig. 6 depicts this phenomenon more clearly. This graph was constructed by considering the frequency of masses of particles less than the specified size. Both particle types demonstrate comparable behavior: at high temperatures, larger particles are required to achieve the same mass contribution beyond 45%, whereas finer ones are needed for mass contributions below 45%. This observation implies an enlargement of the aerosol size spectrum. Notably, the influence on CsI particles appears to be limited, possibly due to their lower temperature condition of 60 °C, in contrast to the 120 °C of SnO_2 particles. The higher temperature promotes both the agglomeration and de-agglomeration processes in SnO_2 particles. As the AMMD values for SnO_2 particles increased (indicating a size distribution shift towards larger particles), this suggests that the agglomeration effect is more dominant than the de-agglomeration one. This observation is further supported by the results of the 7:3 (SnO_2: CsI) mixture, in which d_{max} increased. For pure CsI particles, it appears that the effects of agglomeration and de-agglomeration counterbalance each other, resulting in no significant change in the aerosol size spectrum with increasing temperature. In the case of the 4:6 (SnO_2: CsI) mixture, the observed decrease in d_{min} at a high temperature is more likely attributed to the presence of SnO_2 particles in the mixture, which enhances the de-agglomeration effect. At a high temperature, the presence of SnO_2 in the mixture upsets the equilibrium between the agglomeration and de-agglomeration rates of CsI, creating a new balance that enables the de-agglomeration effect to be quantified.

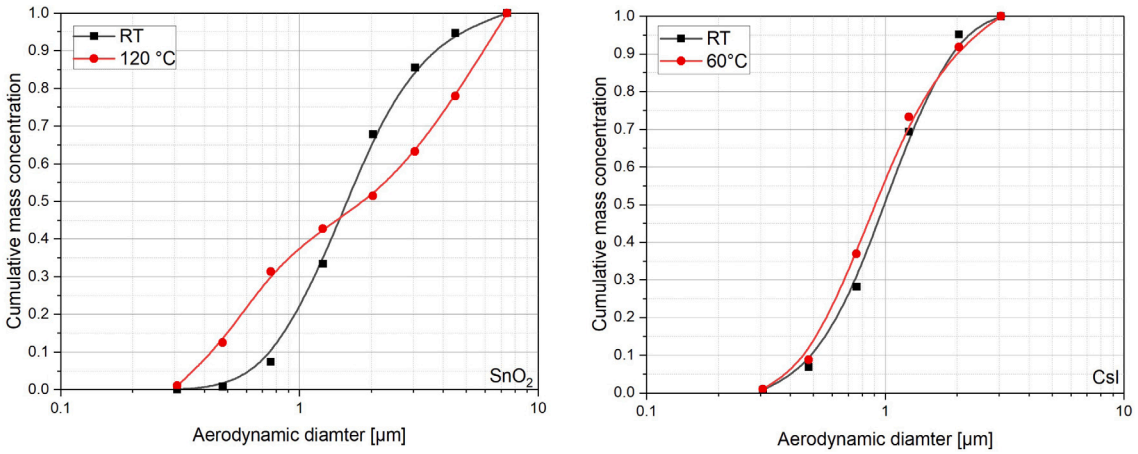

Fig. 6. Comparing the cumulative mass distribution of SnO_2 (left) and CsI (right) at two different temperatures under medium humidity and atmospheric pressure.

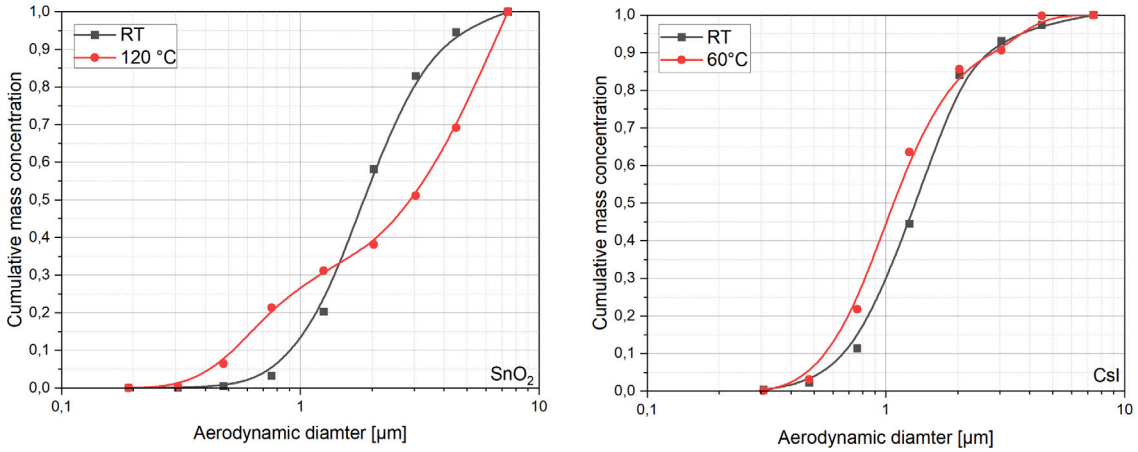

Fig. 7. Comparing the cumulative mass distribution of SnO_2 (left) and CsI (right) at two different temperatures under medium humidity and atmospheric pressure after 1 h depletion.

Consequently, the size spectrum of the SnO_2 aerosol becomes broader as the temperature increases. However, the presence of CsI in the mixture may suppress or inhibit this expansion. Fig. 7 displays the accumulated mass distribution after aerosol depletion over a period of one hour. Whether it is SnO_2 particles or CsI particles, the trend of the temperature-influenced distribution plot of both aerosols after 1 h of depletion is similar to the previously mentioned phenomena. This further validates the influence of temperature on the change in aerosol size spectrum.

3.2. Pressure

In order to maintain a controlled pressure level during the aerosol experiments, a PID pressure valve was utilized. The valve remained closed until the desired pressure was reached, and was then gradually opened to regulate and stabilize the pressure at the desired level. This approach ensured that the injection process for the pressure tests was dynamically balanced, allowing for precise control and maintenance of the desired pressure throughout the experiment. In the IN–EX experiments, two different gauge pressures, namely 3 bar and 6 bar, were tested. The AMMD, GSD, d_{min}, and d_{max} were also calculated and are displayed in Table 4. Comparatively, the values of AMMD and GSD are generally higher at 3 bar, except for the case of SnO_2.

The aerosol size spectrum change resulting from the impact of pressure is plotted in Fig. 8. For pure SnO_2 aerosols, there does not appear to be a significant change in the values of d_{min} and d_{max}. Although there is a tendency towards an increase in d_{max}, the overlapping error margins suggest that the differences may not be statistically significant. In contrast, for pure CsI aerosols, it is observed that d_{max} decreased and d_{min} remains unchanged, indicating a shift in the aerosol size spectrum towards smaller particles. The mixtures exhibit a similar phenomenon as CsI, with a decrease in the d_{min} value as well.

The observed phenomena can be attributed to the compression of aerosols under pressure, which leads to a decrease in particle size and, consequently, a shift towards smaller particles in the distribution. Meanwhile, the particles' movement becomes more rapid, increasing the likelihood of collisions. In particular, for aggregate clusters, these collisions can cause the clusters to break up, resulting in enhanced de-agglomeration. Liu and Hrenya (2018) mentioned that de-agglomeration commonly occurs with an increase in collisional impact velocity, which can be influenced by both temperature and pressure. To et al. (2009) observed in their measurements that nanoparticle aggregates can be broken at higher pressures, indicating that pressure increase enhances de-agglomeration effects. This breakup of clusters contributes to the reduction in d_{max} and d_{min}, as the larger agglomerates are broken down into smaller particles. These collisions may enhance the agglomeration effect as well, and unlike the temperature influence, the enhanced agglomerates may be compressed to smaller sizes due to the pressure effect, which leads to a decrease in d_{max} and d_{min}. The observations in the mixtures and CsI particles support the aforementioned argument. They show a shift in the aerosol size spectrum towards smaller particles. However, it is noteworthy that the SnO_2 particles did not exhibit the same phenomena, and their aerosol size

Table 4
Impact of pressure[a] on the aerosol size spectrum under the RT and dry conditions.

Material	AMMD/μm		GSD		d_{min}/μm		d_{max}/μm	
	3 bar	6 bar	3 bar	6 bar	3 bar	6 bar	3 bar	6 bar
SnO_2	1.08	1.12	1.75	1.77	0.35 ± 0.007	0.36 ± 0.007	3.31 ± 0.167	3.51 ± 0.182
7:3	1.65	1.23	1.87	1.82	0.47 ± 0.004	0.37 ± 0.003	5.77 ± 0.295	4.07 ± 0.214
4:6	1.65	1.31	1.81	1.76	0.50 ± 0.0006	0.42 ± 0.0004	5.41 ± 0.279	4.06 ± 0.216
CsI	1.51	1.31	1.58	1.52	0.60 ± 0.009	0.57 ± 0.008	3.77 ± 0.197	3.03 ± 0.164

[a] Pressure refers to gauge pressure.

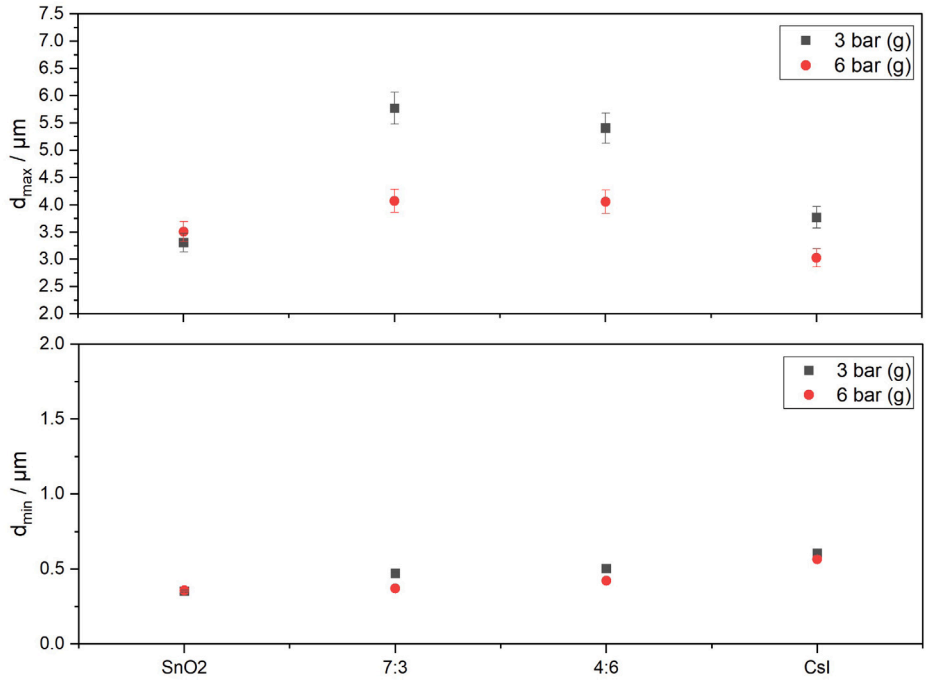

Fig. 8. Comparing the aerosol size thresholds at two different pressures under RT and dry conditions.

did not appear to be influenced by the changes in pressure. Although measurement error could be a potential explanation, the consistent results obtained from all three replicated tests suggest otherwise. Fig. 9 has been plotted to provide insight into the aforementioned distribution shifting to smaller particles. The diagram illustrates a comparison of cumulative mass distributions between SnO_2 (left) and CsI (right) under two different pressures. When analyzing SnO_2 particles, it was observed that there is no size shift between 3 bar and 6 bar. This suggests that SnO_2, being a solid particle, cannot be further compressed. It forms a dynamic equilibrium between the agglomeration and de-agglomeration processes, leading to no further changes in aerosol size within the pressure range from 3 bar to 6 bar. In the case of CsI particles, a distribution shift towards smaller particles is observed at 6 bar. Moreover, the presence of CsI disrupts the balance between the agglomeration and de-agglomeration effects of SnO_2 particles in the mixture, leading to a shift towards smaller particles. As a result, the aerosol size spectrum becomes narrower as the pressure increases, except for insoluble SnO_2 aerosols. Fig. 10 illustrates the accumulated mass distribution following the depletion of aerosol over a one-hour period. There are minimal discrepancies compared to Fig. 9, whether it pertains to SnO_2 particles or CsI particles. This observation further substantiates the impact of pressure on the alteration of the aerosol size spectrum.

3.3. Relative humidity

Controlling relative humidity in the IN–EX experiments posed a challenge due to the limitations of the steam generator. Achieving and maintaining an exact humidity level becomes impractical under such circumstances. As a solution, it is more feasible to describe the influence of humidity on the changes in the aerosol size spectrum by utilizing a range of humidity (see Section 2). The calculated values for AMMD, GSD, d_{min}, and d_{max} are displayed in Table 5. For CsI particles, the AMMD values increase with increasing relative humidity, except under the condensation condition, under which both the AMMD and GSD for CsI particles display a significant decline. We suspect that the reason for this is that as CsI is soluble, the particles readily interact with the condensed water surface. Before reaching the sampling height (1.5 m), CsI particles may have already settled with the water droplets, preventing them from being captured in the measurement. Therefore, the data for CsI under the condensation condition may not provide valuable information regarding the influence of humidity on the aerosol size spectrum. We do not discuss this in this paper.

The aerosol spectrum changes due to the influence of relative humidity on SnO_2, CsI, and their mixtures, which are presented in Fig. 11. It can be observed that there is an increasing tendency in d_{max} for both SnO_2 and CsI aerosols with increasing humidity. For the mixture of SnO_2 and CsI with a mass composition ratio of 7:3, the d_{max} value at high relative humidity appears to be an outlier, possibly due to measurement error. However, it still demonstrates an obvious increase in d_{max} with increasing humidity, similar to pure substances. For the mixture of SnO_2 and CsI with a mass composition ratio of 4:6, a different result was obtained: as the relative humidity increased, there was a decrease in the d_{max}. In the condensation scenario, the behavior of this mixture resembled that of pure CsI (CsI is dominant in this mixture), where condensed water surface tension plays a dominant role. Due to this effect, it is difficult for the particles to reach

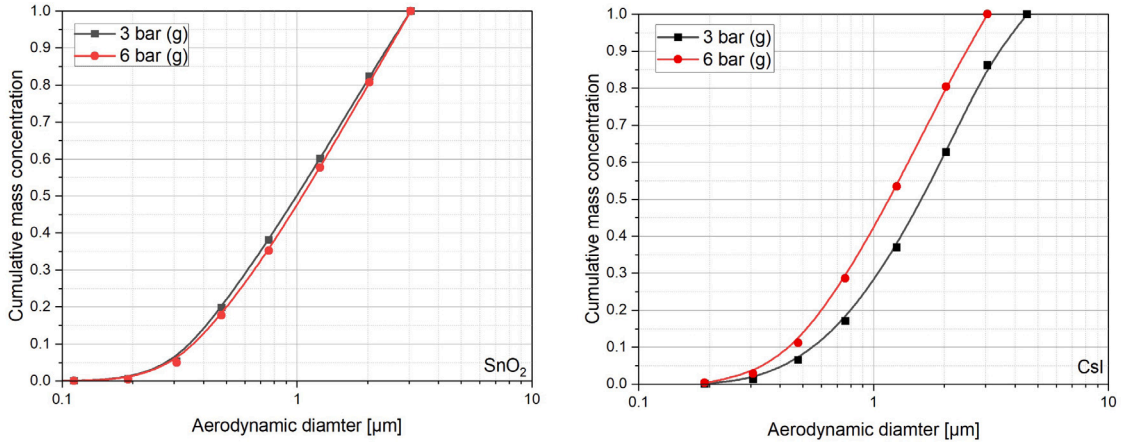

Fig. 9. Comparing the cumulative mass distribution of SnO_2 (left) and CsI (right) at two different pressures under RT and dry conditions.

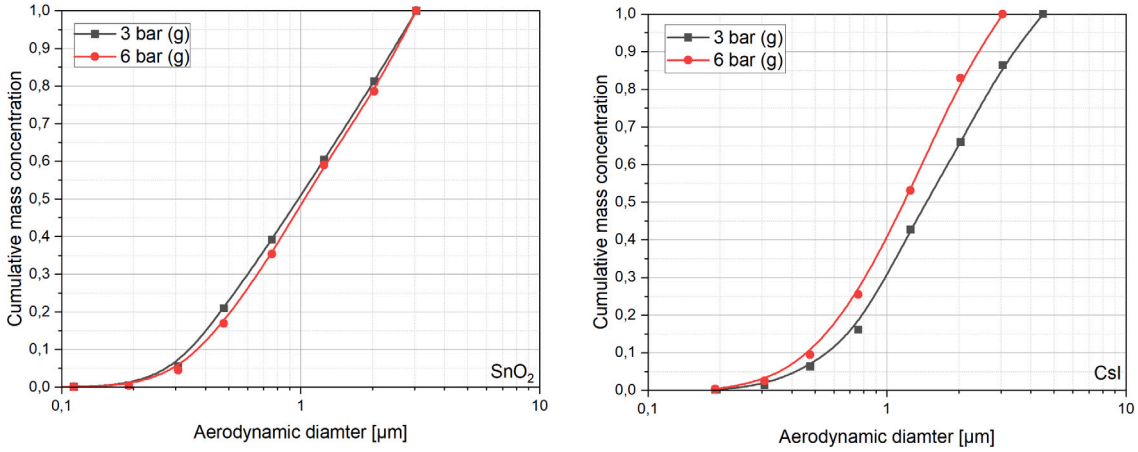

Fig. 10. Comparing the cumulative mass distribution of SnO_2 (left) and CsI (right) at two different pressures under RT and dry conditions after 1 h depletion.

Table 5
Impact of relative humidity on the aerosol spectrum under RT and atmospheric pressure.

Material	AMMD/µm		GSD		d_{min}/µm		d_{max}/µm	
	dry	med	dry	med	dry	med	dry	med
SnO_2	1.67	1.64	1.57	1.60	0.68 ± 0.012	0.64 ± 0.012	4.12 ± 0.208	4.20 ± 0.218
7:3	–	1.45	–	1.63	–	0.55 ± 0.005	–	3.85 ± 0.203
4:6	–	1.37	–	1.60	–	0.54 ± 0.0006	–	3.51 ± 0.187
CsI	1.16	1.20	1.59	1.62	0.46 ± 0.006	0.46 ± 0.007	2.93 ± 0.159	3.15 ± 0.165
Material	high	con	high	con	high	con	high	con
SnO_2	1.72	1.69	1.62	1.69	0.66 ± 0.013	0.59 ± 0.011	4.51 ± 0.228	4.83 ± 0.250
7:3	1.84	1.50	1.74	1.72	0.61 ± 0.006	0.51 ± 0.004	5.57 ± 0.285	4.44 ± 0.228
4:6	1.17[a]	1.17	1.59[a]	1.65	0.46 ± 0.0005	0.43 ± 0.0005	2.96 ± 0.156	3.19 ± 0.165
CsI	1.39	0.51	1.73	1.33	0.46 ± 0.007	0.29 ± 0.004	4.16 ± 0.218	0.90 ± 0.049

[a] The relative humidity conditions for this experiment were between 100% and more than 100%.

the measuring height, as mentioned previously, resulting in the d_{max} decreasing. For high humidity conditions, it is important to highlight that the relative humidity in this test reached levels of 100% and even exceeded it. Consequently, the behavior observed under this "high humidity" condition is similar to that observed in the condensation scenario, with a decrease in the d_{max}.

Fig. 12 illustrates the cumulative mass distribution of SnO_2 and CsI at various relative humidities. For the insoluble particles (SnO_2), it is challenging to observe a shift towards larger particles with an increase in humidity in this diagram. However, relative humidity is a crucial parameter that affects the adhesive forces between aerosol particles. When aerosol particles come into contact with each other, the presence of water vapor in the air can facilitate the formation of liquid bridges between them. These liquid bridges act as adhesive forces, causing the particles to stick together and form agglomerates. Eq. (8) from Hinds (1999) provides a useful expression for estimating the adhesive force between hard materials, such as SnO_2 particles. It can be seen that the extent of agglomeration depends on the relative humidity level. A higher relative humidity provides a greater availability of water vapor, resulting in stronger adhesive forces and potentially larger agglomerates. Hence, the d_{max} values of pure SnO_2 aerosols and the mixture (SnO_2: CsI = 7:3) increases with the rise in relative humidity.

$$F_{adh} = 150d[0.5 + 0.0045(\%RH)] \quad (8)$$

Unlike SnO_2 particles, the CsI size distribution shifts towards large particles with an increase in relative humidity, as shown in Fig. 12.

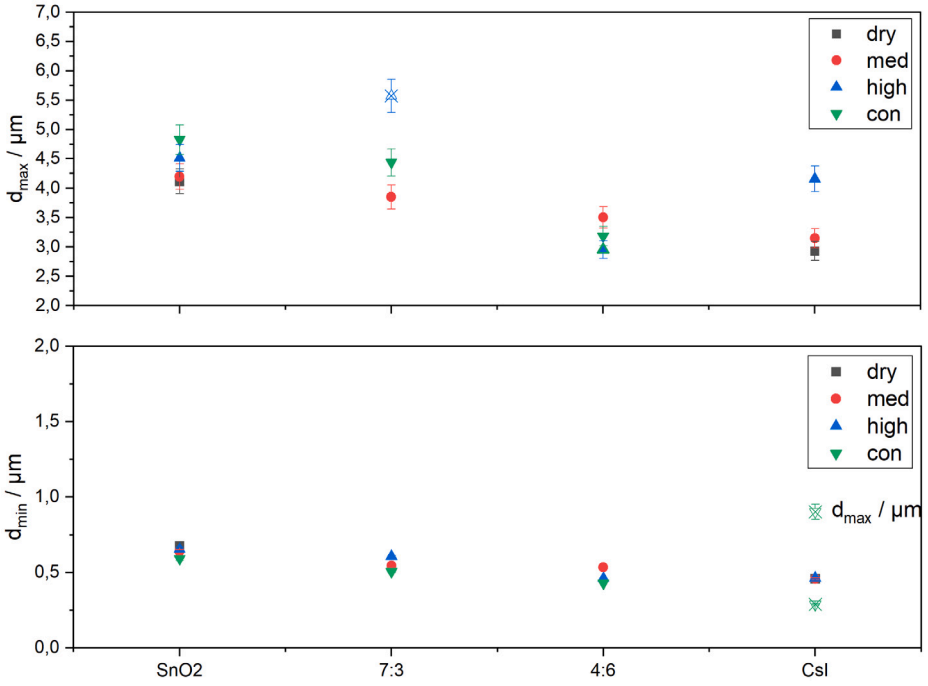

Fig. 11. Comparing the aerosol size thresholds at two different pressures under RT and atmospheric pressure.

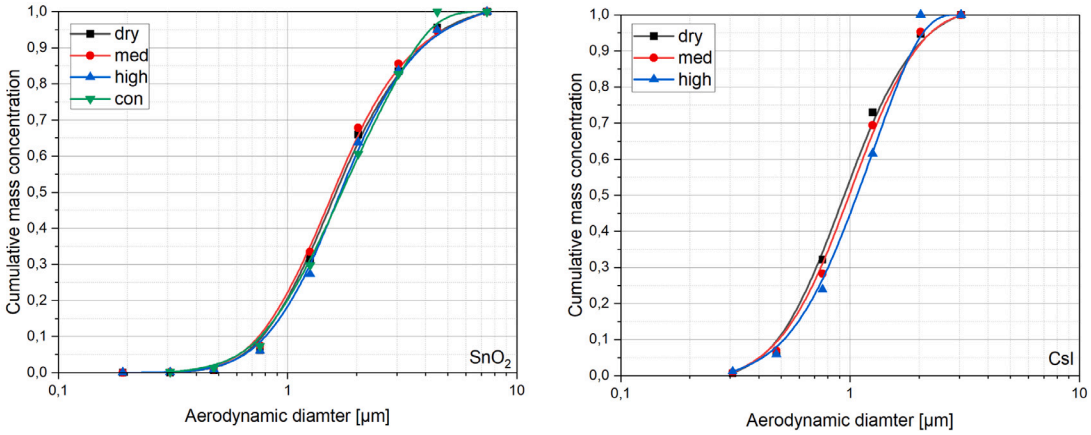

Fig. 12. Comparing the cumulative mass distribution of SnO_2 (left) and CsI (right) at different relative humidities under RT and atmospheric pressure.

This can be attributed to the hygroscopic properties of CsI, which enhance the influence of humidity on the adhesive force between particles, leading to an enhanced agglomeration effect. Additionally, studies conducted by Mishra et al. (2019) have shown that the growth factor for CsI remains constant within the relative humidity range of 30%–90%, further supporting the positive effect of humidity on the agglomeration enhancement of CsI particles. The mixtures exhibit similar results to those observed in pure substances. As a result, the size spectrum of aerosols becomes broader, particularly for insoluble aerosols such as CsI. The Fig. 13, depicting the cumulative mass after one hour of aerosol depletion, provides further validation of the previously mentioned results for both particles.

4. Conclusion

A series of experiments were performed using an IN–EX facility, and the results have been analyzed to discuss the effects of temperature, pressure, and relative humidity on the changes in the aerosol spectrum of SnO_2, CsI, and their mixtures.

Increasing the temperature results in higher particle kinetic energy and an increased possibility of particle collisions, leading to enhanced agglomeration and de-agglomeration processes. As a result, the aerosol spectrum of SnO_2 particles becomes broader with increasing temperatures. However, for CsI aerosols, the enhancement of de-agglomeration and agglomeration appears to be counterbalanced. The presence of CsI in the mixture may act to suppress or inhibit the expansion of the aerosol size spectrum.

Under pressure conditions, particles move more rapidly and have higher collision rates, causing the breakup of aggregates and increased de-agglomeration. Meanwhile, the agglomeration rate is also enhanced. The aggregates may be compressed to smaller sizes under continuous pressure. As a result, the aerosol size spectrum of CsI particles and mixtures shifts towards smaller particles. However, in the case of SnO_2 particles, the enhanced de-/agglomeration effects reach an equilibrium, resulting in no significant changes in the size spectrum with pressure

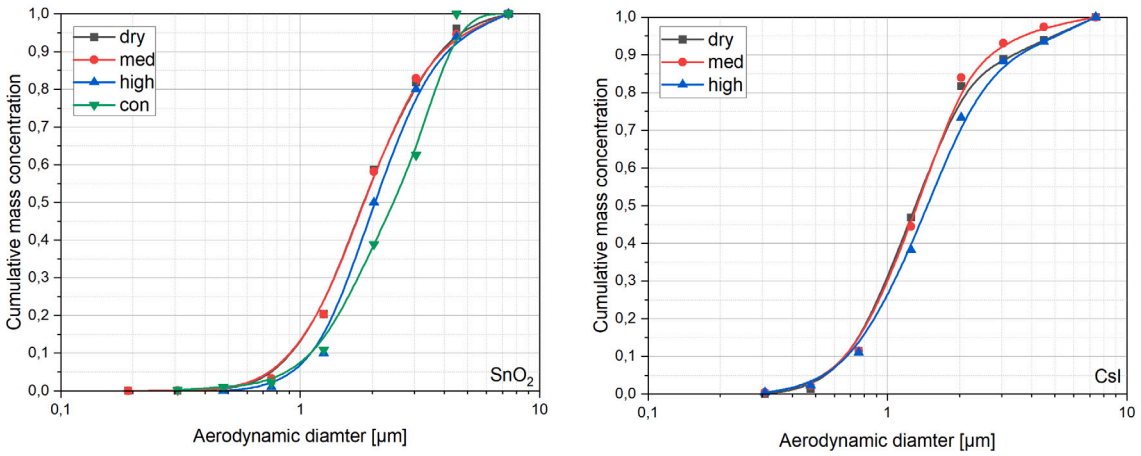

Fig. 13. Comparing the cumulative mass distribution of SnO_2 (left) and CsI (right) at different relative humidities under RT and atmospheric pressure after 1 h depletion.

variations. The presence of CsI in the mixture can disrupt this balance and cause a shift in the size spectrum towards smaller particles.

With increasing relative humidity, the adhesive force between solid particles improves, leading to enhanced agglomeration. As a result, the aerosol size spectrum of SnO_2 and CsI aerosols shifts towards larger particles. Due to the hygroscopic property of CsI, the effect of the size spectrum's expansion becomes even more pronounced.

The experiment yields valuable insights into aerosol behavior by illuminating the changes in the aerosol size spectrum under different thermodynamic conditions. This information can be practically applied in severe accident scenarios. For instance, increasing the humidity inside the containment can be considered a strategy for shifting the aerosol spectrum towards larger particles. This approach aims to enhance the settling rate of aerosols, thereby reducing the risk of their release into the environment. Nevertheless, it is important to note that all the findings presented here are derived from our experimental data. To offer additional evidence supporting our conclusion about the de-/agglomeration effects, it certainly would be desirable to conduct theoretical assessments based on molecular dynamics theory in the future.

CRediT authorship contribution statement

Y. Wu: Writing – original draft, Visualization, Validation, Investigation, Formal analysis, Data curation. **M. Klauck:** Writing – review & editing, Supervision, Project administration, Methodology. **K. Trollmann:** Writing – review & editing, Formal analysis, Conceptualization. **H.-J. Allelein:** Supervision, Project administration, Funding acquisition.

Declaration of competing interest

The authors declare that they have no known competing financial interests or personal relationships that could have appeared to influence the work reported in this paper.

Data availability

Data will be made available on request.

Acknowledgments

Parts of this work were funded by the German Federal Ministry for the Environment, Nature Conservation, Nuclear Safety and Consumer Protection (BMUV, grant No. 1501551) on the basis of a decision by the German Bundestag.

References

Davies, C.N., 1968. The entry of aerosols into sampling tubes and heads. J. Phys. D: Appl. Phys. (ISSN: 0022-3727) 1 (7), 921–932. http://dx.doi.org/10.1088/0022-3727/1/7/314, https://iopscience.iop.org/article/10.1088/0022-3727/1/7/314.

Dehbi, A., Suckow, D., Guentay, S., 1997. The effect of liquid temperature on pool scrubbing of aerosols. Arerosol Sci. 28, 2.

Firnhaber, M, Fischer, K, Schwarz, S, Weber, G, Dienstbier, Jiri, 2002. International Standard Problem ISP44-KAEVER-Experiments on the Behavior of Core-melt Aerosols in a LWR Containment Comparison Report. Report, Organisation for Economic Co-Operation and Development-Nuclear Energy Agency.

Firnhaber, M., Kanzleiter, T.F., Schwarz, S., Weber, G., 1996. International Standard Problem ISP37: VANAM M3 - A Multi Compartment Aerosol Depletion Test with Hygroscopic Aerosol Material: Comparison Report. Report, URL http://inis.iaea.org/search/search.aspx?orig_q=RN:41025229.

Fromentin, A., Haschke, D., Taubenberger, R., Schikarski, W., Schoeck, W., Bunz, H., Kanzleiter, T., Schroeder, T., Peehs, M., Ruhmann, H., Fischer, M., Weber, G., Jahn, H., 1988. Demona (demonstration of nuclear aerosol behavior) - study of aerosol behavior in a containment. J. Aerosol Sci. (ISSN: 0021-8502) 19 (1), 65, URL.

Gupta, S., 2017. Main Insights and Perspectives of Pool scrubbing Research: Examples of THAI and NUGENIA/IPRESCA. In: PASSAM Final Workshop on source term mitigation of severe accidents.

Gupta, S., Schmidt, E., von Laufenberg, B., Freitag, M., Poss, G., Funke, F., Weber, G., 2015. THAI test facility for experimental research on hydrogen and fission product behaviour in light water reactor containments. Nucl. Eng. Des. (ISSN: 0029-5493) 294, 183–201. http://dx.doi.org/10.1016/j.nucengdes.2015.09.013, URL.

Hinds, William C., 1999. Aerosol Technology: Properties, Behavior, and Measurement of Airborne Particles. John Wiley & Sons, ISBN: 0471194107.

Kanzleiter, T., Fischer, K.O., Allelein, H.J., Schwarz, S., Weber, G., 1991. The vanam experiments M1 and M2 - test-results and multicompartmental analysis. J. Aerosol Sci. (ISSN: 0021-8502) 22, S697–S700, URL.

Keskinen, J., Pietarinen, K., Lehtimaki, M., 1992. Electrical low-pressure impactor. J. Aerosol Sci. (ISSN: 0021-8502) 23 (4), 353–360.

Kim, Min Young, Bang, Young Suk, Park, Tong Kyu, Lee, Doo Yong, Lee, Byung Chul, Park, Sung Hoon, 2016. Containment aerosol characterization during nuclear power plant severe accident. Particul. Sci. Technol. (ISSN: 0272-6351) 34 (5), 622–632. http://dx.doi.org/10.1080/02726351.2015.1099066.

Kobalz, J., Allelein, H.-J., 2017. SAAB Test Facility – Separate Effect Tests on Pool Scrubbing Phenomena. In: PASSAM Final Workshop on source term mitigation of severe accidents.

Li, Yu, Gu, Weiguo, Wang, Dezhong, He, Jinpeng, 2018. Direct numerical simulation of polydisperse aerosol particles deposition in low Reynolds number turbulent flow. Ann. Nucl. Energy (ISSN: 0306-4549) 121, 223–231. http://dx.doi.org/10.1016/j.anucene.2018.07.034, URL https://www.sciencedirect.com/science/article/pii/S0306454918303839.

Lind, T., Ammar, Y., Dehbi, A., Guntay, S., 2010. De-agglomeration mechanisms of TiO2 aerosol agglomerates in PWR steam generator tube rupture conditions. Nucl. Eng. Des. (ISSN: 0029-5493) 240 (8), 2046–2053. http://dx.doi.org/10.1016/j.nucengdes.2010.03.002.

Liu, P., Hrenya, C.M., 2018. Cluster-induced deagglomeration in dilute gravity-driven gas-solid flows of cohesive grains. Phys. Rev. Lett. 121 (23), 238001. http://dx.doi.org/10.1103/PhysRevLett.121.238001, (ISSN: 1079-7114 (Electronic) 0031-9007 (Linking)). URL https://www.ncbi.nlm.nih.gov/pubmed/30576183.

Ltd., Dekati, 2018. Dekati® High Pressure Diluter DEED-300 Brochure. Dekati Ltd..

Mishra, G., Mandariya, A.K., Tripathi, S.N., Mariam, Joshi, M., Khan, A., Sapra, B.K., 2019. Hygroscopic growth of CsI and CsOH particles in context of nuclear reactor accident research. J. Aerosol Sci. (ISSN: 0021-8502) 132, 60–69. http://dx.doi.org/10.1016/j.jaerosci.2019.03.008, URL.

Scheibel, H.G., Poss, G., Weber, D., 1992. Kaever: an experiment for an improved understanding of aerosol depletion processes in a reactor containment. J. Aerosol. Sci. 23, S209–S212.

Scheibel, H.G., Poss, G., Weber, D., 1993. Influence of aerosolparameters on the aerosol behaviour in reactor containments- first results of the project kaever. J. Aerosol. Sci. 24, S305–S306.

Scheibel, H.G., Poss, G., Weber, D., 1994. First results of the kaever project on aerosol behaviour in LWR containments. J. Aerosol. Sci. 25, S95–S96.

To, Daniel, Dave, Rajesh, Yin, Xiaolong, Sundaresan, Sankaran, 2009. Deagglomeration of nanoparticle aggregates via rapid expansion of supercritical or high-pressure suspensions. AIChE J. 55 (11), 2807–2826. http://dx.doi.org/10.1002/aic.11887, (ISSN: 0001-1541 1547-5905).

Wu, Y., Klauck, M., Allelein, H.J., Experimental investigation on the depletion behavior of multi-component aerosols. In: 20th International Topical Meeting on Nuclear Reactor Thermal Hydraulics (NURETH-20). American nuclear society.

Wu, Y., Klauck, M., Allelein, H.J., 2022a. Experimental investigation on the impact of different thermodynamic parameters on the depletion behavior of nuclear aerosols in the IN-EX facility. Nucl. Eng. Des. (ISSN: 00295493) 397, http://dx.doi.org/10.1016/j.nucengdes.2022.111912.

Wu, Y., Klauck, M., Allelein, H.J., 2022b. Experimental investigation on the interaction behavior of nuclear aerosols with cable fire products. In: The 13th International Topical Meeting on Nuclear Reactor Thermal-Hydraulics, Operation and Safety (NUTHOS 13).

Ziegler, Albert, Allelein, Hans-Josef, 2013. Reaktortechnik: Physikalisch-Technische Grundlagen. ISBN: 978-3-642-33845-8.